DEPARTMENT OF PHYSICS

LUDWIG-MAXIMILIANS-UNIVERSITÄT MÜNCHEN

Numerical Analysis of the Min-System in the *in vivo* Parameter Regime

Investigation of how Changes in Particle Density Ratios Affect the Wavelength Selection of Pattern Formation in the Skeleton Model

Laura Kern

DEPARTMENT OF PHYSICS

LUDWIG-MAXIMILIANS-UNIVERSITÄT MÜNCHEN

Numerical Analysis of the Min-System in the *in vivo* Parameter Regime

Investigation of how Changes in Particle Density Ratios Affect the Wavelength Selection of Pattern Formation in the Skeleton Model

Report für das Forschungspraktikum am Lehrstuhl Frey

Authors: Laura Kern
Supervisor: Laeschkir Würthner, Raphaela Geßele
Advisor: Prof. Dr. Erwin Frey

I confirm that this report is my own work and I have documented all sources and material used.

Munich, 7.02.2020 Laura Kern

Acknowledgments

I am grateful to Prof. Dr. Frey for giving me the opportunity to join the group for a research internship.

I especially want to thank Laeschkir and Raphaela for their extraordinary support. I really appreciate the valuable conversations which taught me a lot about how to approach the intricate yet fascinating topic of non-linear dynamics and pattern formations. Besides the new skills I learned, this internship also sparked a great interest in this field of research.

Abstract

Cells are the fundamental building blocks of life. Many important cell processes rely on robust self-organized spatial patterning by proteins. Studying the dynamics of the Min-system[1][2] in *E.coli* is a very valuable example of such spatio-temporal patterns. Oscillations of MinD and MinE proteins result in a time-averaged concentration minimum in the middle of the cell which localizes the site for cell division.

This report investigates how the skeleton model[1] of the Min-system responds to changes in protein density ratios within the *in vivo* parameter regime.

The simulations show that short wavelength modes, as predicted by linear stability analysis, can occur due to changes in protein density ratios. However theses modes are very unstable and quickly decay back into coherent standing wave patterns.

This shows that the skeleton model is remarkably robust in adapting to changes in protein ratios and still retains the ability to locate the middle of the system.

In the attempt to interpret this behaviour, linear stability analysis (LSA) revealed that the fastest growing mode q_c determined by the integer mode number n_c and the largest unstable mode q_{max} determined by n_{max} are always commensurable i.e. $q_{max} = m \cdot q_c$ with $m \in \mathbb{N}^*$. In search for a theoretical framework to explain the transitions between turbulence and coherent patterns far away from the global equilibrium the commensurability between unstable modes seem to play an important role[3].

Even though the predictions of LSA are consistent at the onset of pattern formation, LSA is not capable of sufficiently describing the long term behaviour of the system. The non-linear interactions of the unstable modes appear to dominate the long-time behaviour of the system.

Contents

1. Introduction and Motivation

1.1. The Min-System

A cell is the smallest unit of living organisms. Prokaryotic cells like bacteria depend on intracellular processes and in turn, these intracellular processes rely on robust self-organized spatial patterning by proteins[4].

The Min-system in *E.coli* is a common model for studying such dynamics. *E.coli* is a rod-shaped bacterium. Oscillations of MinD and MinE proteins result in a time-averaged concentration minimum in the center of the cell which localizes the site for cell division exactly in its middle. The spatio-temporal dynamics of these proteins can be seen in *in vivo* experiments[5] (see Fig.1.1).

The aim of modelling the Min-system is to identify what biochemical core mechanisms of *E.coli* cells result in self-organized intracellular pattern formation.

A good model has to capture the complexity of the system while keeping it simple enough to maintain tractability.

1.2. Modelling the Min-System

This work follows the skeleton model of the Min-system proposed by Halatek and Frey[1] which is based on two protein species MinD and MinE. This skeleton model is a five component, mass conserving reaction diffusion system (see Fig.2.2).

Experiments were performed *in vitro*, where the two protein species MinD and MinE along with ATP were put into an aqueous solution with a supported lipid bilayer at the bottom. Strikingly, the proteins also form complex spatio-temporal patterns[6][7] on the membrane similar to what has been observed on a theoretical level. These *in vitro* experiments provide a good foundation to compare with theory.

The skeleton model can produce patterns observed in *in vivo* and in *in vitro* experiments by identifying underlying mechanisms that governing both regimes. Both MinD and MinE can *attach* and *detach* from the membrane. MinD can undergo *nucleotide exchange* to change between an MinD-ADP and a MinD-ATP state as well as *recruiting* other MinD to the membrane (see Chapter 2.1.2 for more detail). Establishing these common mechanisms for both the *in vivo* and in *in vitro* regime makes it a very promising model.

Protein patterning mechanisms can handle differences in protein numbers without disrupting core function. The robustness of the Min-system for a wide range of MinE/MinD denisity ratios has been observed in *in vitro* experiments[6]. However, the skeleton model is not able to capture this robustness feature because it only predicts patterns when there is fewer MinE

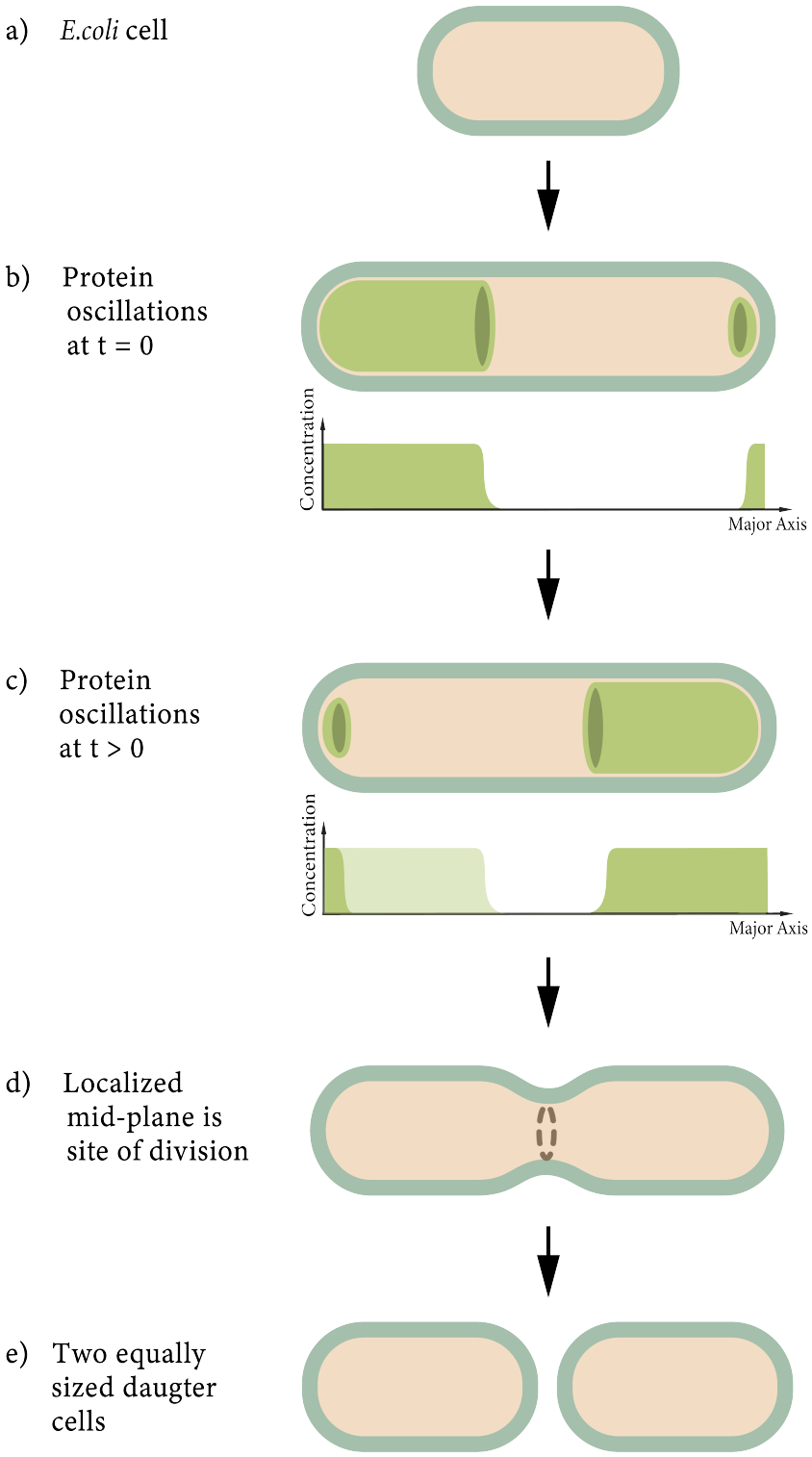

Figure 1.1: Schematic representation of how the site for division in localized.
a) *E.coli* cell grows before dividing into two daughter cells.
b) MinD polar zone (bright green) grows on the left side of the major axis of the cell, thereby increasing MinD concentration in the left polar region. A smaller polar zone of MinD starts to grow on the right pole of the cell.
c) As the left polar zone is depleted, the right polar region starts to grow due to an oscillation of particles from one pole to the other in the system, thereby increasing MinD concentration on the right pole of the cell. The time-average of MinD concentrations along the major axis localize the mid-plan.
d) At the concentration minimum a contraction ring is formed.
e) The contraction ring in the middle of the cells divides one cell into two equally sized daughter cells

than MinD. Based on biochemical findings[8], an extension of the skeleton network was proposed by Denk[2]. The new model introduces a conformational switch in MinE which allows the model to predict patterns even if MinE is more abundant than MinD. The switch model was not considered in this numerical study. It is an extension of the skeleton model which should be fully understood in the *in vivo* regime first. However the switch model is described in more detail in the Outlook-chapter 4.2.3.

1.3. Motivation of this Work

In recent experiments it was noticed that in *in vivo* dynamics, the wavelength selection of the patterns is correlated with the amount of MinE in the system[9]. The objective of this work is to investigate whether higher modes become linearly unstable and dominate the long-time behavior as particle densities are varied in the system in the *in vivo* parameter regime. This will further the understanding of how the skeleton model responds to changes in MinE/MinD denisity ratios.

The enormous parameter space of the system as well as the lack of experimentally verified parameters render it difficult for the model to make precise predictions. Any comparison of the model with experiments is only qualitatively not quantitatively.

In order to find relevant parameters worth simulating the full dynamics, the method of linear stability analysis (LSA) is applied. LSA makes no assertions about the pattern. Rather, it is the study of the time evolution of small perturbations with respect to stationary homogeneous solutions. Parameter regimes exhibiting growing modes are good candidates for pattern formation[10]. These sets of parameters are then used to simulate the system. The simulation of the density profile for the membrane species gives an indication on whether the resulting patterns can arise by changes in MinE/MinD density ratios.

LSA can predicts the patterns at onset but not for longer times. Non-linearities always have a crucial impact on the dynamics and in the case of the skeleton model, the non-linear interactions of the unstable modes dominate the long-time behaviour of the system. The linear terms predicted by LSA become less significant as the patterns evolves in time.

According to the hypothesis of Halatek and Frey, transitions between turbulence and coherent patterns arbitrary far away from the global equilibrium may be related to commensurable unstable modes[3]. They showed that that the fastest growing mode q_c and the largest unstable mode q_{max} are commensurable such that $q_{max} \geq 2 \cdot q_c$. The two unstable modes have distinct yet independent roles in the establishment of global coherence.

As a next step, the skeleton model can be further investigated under different boundary conditions. This might aid in exploring the role of unstable commensurable modes in pattern formation away from the global equilibrium. In order to see how changes in particle density ratios affect wavelength selections in *in vivo* parameter regimes it would be important to compare the skeleton model to the amended switch model. This comparison would help to see if the conformational switches in MinE plays a major role in *in vivo* cells.

2. Background

2.1. Skeleton Model of the Min-system

2.1.1. Localizing the Middle of a Rod-Shaped Cell

There are several proteins involved in the process of cell division. However, in order to understand how the rod-shaped bacterium *E.coli* locates the middle of its cell, only two main proteins are of interest, namely MinD and MinE. Pole-to-pole oscillations by these two proteins result in a time-averaged concentration minimum in the center of the cell which localizes the site for cell division exactly in the middle (see Figure 1.1). The pole-to-pole oscillations of MinD were observed in *in vivo* experiments[5] as well as in *in vitro* experiments [7].

2.1.2. Core Mechanisms

In order to understand how the system exhibits dynamics, a microscopic skeleton model was proposed[1]. According to this model, there are four main mechanisms responsible for the oscillations: *attachment*, *detachment*, *nucleotide exchange* and *recruitment* (see Figure 2.1).
These mechanisms emerge from interactions of the two proteins MinD and MinE at the membrane.. The MinD protein, exhibits different properties depending on which nucleotide is bound to it: Cytosolic MinD-ATP has the ability to *attach* to the membrane; whereas MinD-ADP cannot bind to the membrane and therefore can solely exist in the cytosol.
MinE can bind to the membrane bound MinD-ATP to form a MinDE-complex. MinE catalyses the hydrolysis to turn MinD-ATP to MinD-ADP, which can no longer bind to the membrane, thereby *detaching* from it. MinE will cycle back in the cytosol, whereas MinD-ADP can undergo *nucleotide exchange* in the cytosol to turn back into MinD-ATP, which again has the ability to bind to the membrane again. As soon as MinD-ATP is bound to the membrane it *recruits* more MinD-ATP from the cytosol, which results in the formation of a polar zone. However, this polar zone is depleted by MinE attaching onto it while at the same time a new polar zone on the opposite side is starting to develop due to particle redistribution in the system.

2.1.3. Intracellular Pattern Formation

Intracellular pattern formation is a result of the localized accumulation of proteins on the membrane. Patterns occur when mass distributions of membrane-bound proteins encounter biochemical interactions. When mass redistribution and biochemical interactions balance each other out, the system exhibits lateral instabilities[10].

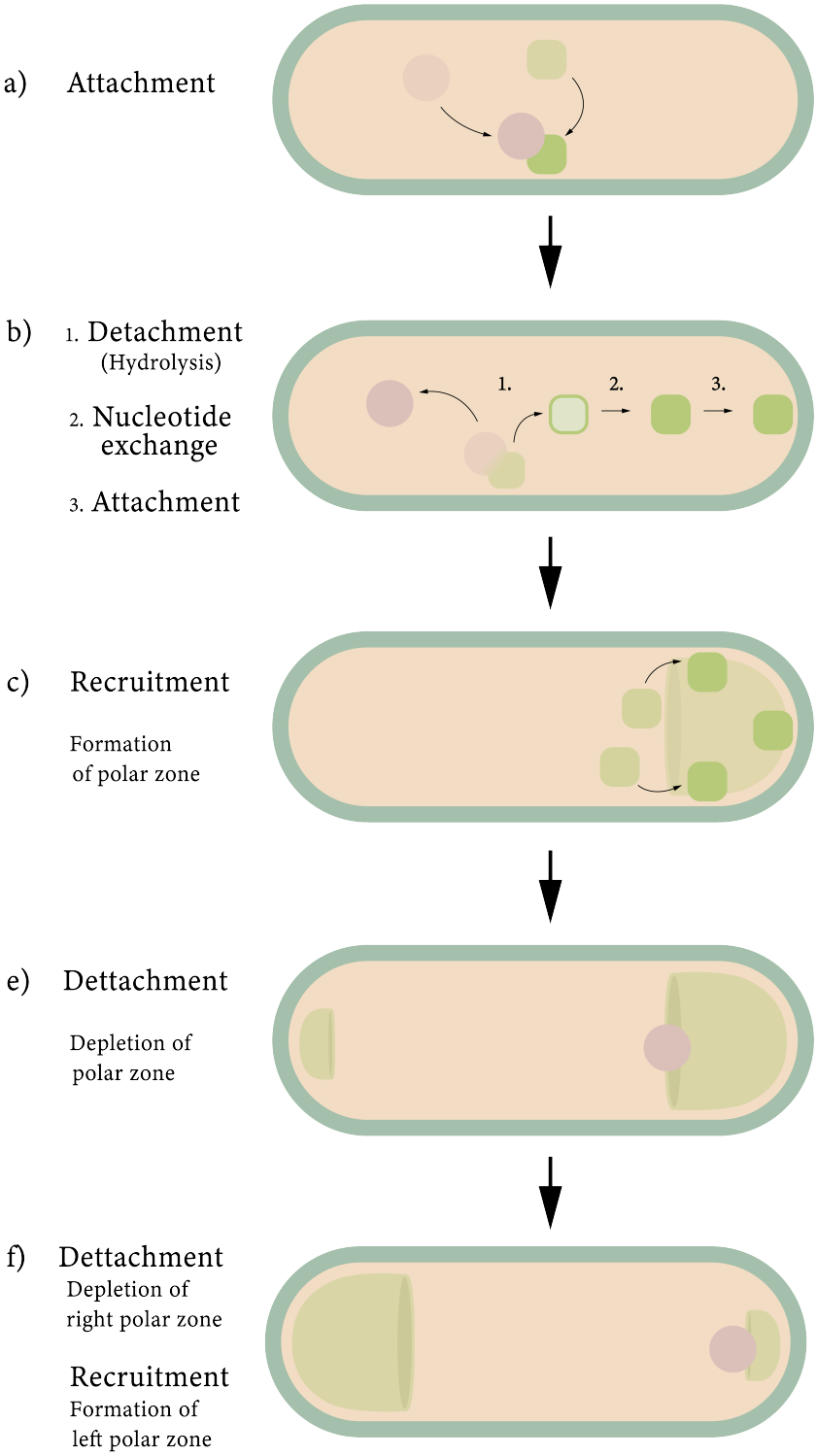

Figure 2.1: This is a schematic representation of how the core mechanism behind Min-oscillations work.
a) MinD-ATP (solid green) *attaches* to the membrane. MinE (pink) attached to membrane bound MinD-ATP to form a MinDE-complex
b) 1. Through hydrolysis in the MinDE-complex MinD-ATP turns into MinD-ADP (light green) which *detaches* from the membrane and MinE is cycled back into the cytosol.
2. Through *nucleotide exchange* MinD-ADP turns back into MinD-ATP.
3. MinD-ATP has the ability to once more attach to the membrane
c) Membrane bound MinD-ATP has the ability to *recruit* more MinD-ATP from the cytosol to attach onto the membrane, thereby forming a polar zone.
d) The polar zone is depleted by MinE attaching to its edges
e) While one polar zone is depleted another polar zone on the opposite side starts to grow due to particle conservation of the system.

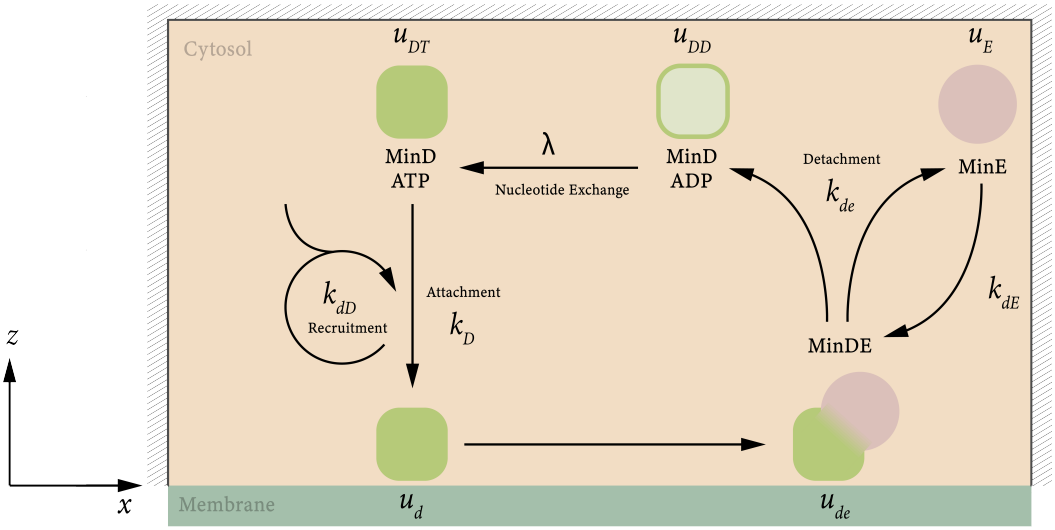

Figure 2.2.: The figure shows a schematic of skeleton model for the Min-system in 2D box geometry with no-flux boundary conditions. The five components are: cytosolic MinD-ADP (u_{DD}) and MinD-ATP (u_{DT}), membrane bound MinD-ATP (u_d) and MinDE-complexes (u_{de}), and cytosolic MinE (u_E). All rates and densities are listed in the glossary.

For dynamical patterns, like in the Min-system, patterns emerges from direct transport. Due to direct transport the formation of spatially separated attachment and detachment zones are established. These zones are coupled though cytosolic gradients in the bulk that facilitate mass redistribution through diffusion.

2.1.4. Mass Conserving Reaction-Diffusion Equations of the Min-System

The interplay of the core mechanisms (2.1.2) of the skeleton model lead to spatio-temporal dynamics i.e. pattern form due to the redistribution of membrane bound proteins.

Dynamics based on conformational switching conserve the number of proteins. Therefore mass conserving reaction-diffusion systems are the appropriate framework for this work. Additionally, in biological systems, particle numbers are constant on the time scale of the pattern. (reff?)

Next, lets look at the equations that describe the system according to Fig.2.2 in a simplified 2D Box geometry.

Diffusion and nucleotide exchange can occur everywhere in the 2D cytosol, while all other reactions can only take place on the membrane surface at $z = 0$. The set of differential equations reads:

For the bulk:

$$\partial_t u_{DD} = D_c \nabla^2 u_{DD} - \lambda u_{DD} \tag{2.1}$$

$$\partial_t u_{DT} = D_c \nabla^2 u_{DT} + \lambda u_{DD} \tag{2.2}$$

$$\partial_t u_E = D_c \nabla^2 u_E \tag{2.3}$$

For the membrane:

$$\partial_t u_d = D_m \nabla^2 u_d + \underbrace{k_D u_{DT} + k_{dD} u_d u_{DT} - k_{dE} u_E u_d}_{f_d} \tag{2.4}$$

$$\partial_t u_{de} = D_m \nabla^2 u_{de} + \underbrace{k_{de} u_E u_d - k_{de} u_{de}}_{f_{de}} \tag{2.5}$$

Note that the symbols for the equations are listed in the glossary. For dynamics to emerge, two conditions have to be fulfilled, namely $k_{dE} > k_{dD}$ and number if MinE < MinD[1].

These equations are complemented by a set of boundary conditions at the membrane and on the sides and top of the box.

The boundary conditions are of great significance since they are responsible for coupling the dynamics of the bulk with the membrane. They account for the exchange of proteins between the cytosol and the membrane.

In mass conserving reaction diffusion systems, the boundary conditions do not allow for particles to leave or enter the domain. Mathematically this implies no-flux boundary conditions as well as constant total particle number in the system. With no particles being created or annihilated, there are only transitions between different states. This results in the reaction terms of the membrane Eq.2.4-2.5 being equal to the reactive or flux boundary conditions on the membrane Eq.2.6-2.8 but with opposite signs.

At the membrane, the requirement is that the flux onto the membrane must be equal to the reaction terms that generate that very same flux. This requires reactive boundary conditions:

$$D_c \nabla u_{DT} \mid_{z=0} = -u_{DT}(k_D + k_{dD} u_d) \tag{2.6}$$

$$D_c \nabla u_{DD} \mid_{z=0} = k_{de} u_{de} \tag{2.7}$$

$$D_c \nabla u_E \mid_{z=0} = k_{de} u_{de} - k_{dE} u_E u_d \tag{2.8}$$

At the top and the sides of the box, there is no flux. This results in the following no-flux

boundary conditions:

$$D_c \nabla u_{DT} \mid_{z=h} = 0 \tag{2.9}$$

$$D_c \nabla u_{DD} \mid_{z=h} = 0 \tag{2.10}$$

$$D_c \nabla u_E \mid_{z=h} = 0 \tag{2.11}$$

Non-linearities only occur on the membrane (Eq.2.4 - 2.5 and Eq.2.6-2.8) but not in the bulk as proteins do not interact in the cytosol.

Mass conservation means that the total number of MinE (N_E) and MinD (N_D) must be constant for all times. The total particle number N_E and N_D are obtained by integrating over all particle densities living in the entire cytosolic volume $\int_\Omega dc$ and on the whole membrane surface $\int_{\delta\Omega} dm$.

$$\begin{aligned} N_D &= \int_\Omega dc(u_{DD} + u_{DT}) + \int_{\delta\Omega} dm(u_d + u_{de}) = \int_\Omega dc\, minD \\ N_E &= \int_\Omega dc\, u_E + \int_{\delta\Omega} dm\, u_{de} = \int_\Omega dc\, minE \end{aligned} \tag{2.12}$$

Model definitions like these, which are independent of the coordinate system, are very useful as changing system geometry does not affect spatial densities of *minE* and *minD*. This very model can be used for different geometries without having to account for mass conservation separately.

2.1.5. System Geometry

Geometry is an important factor for pattern formation. Experiments found that a range of patterns can form in the same system geometries[11]. The conclusion is that intracellular Min-protein patterns are multi-stable and can form a variety of intrinsic length scales. The dependence of pattern formation and cell geometry is linked to the flux coupling between attachment and detachment zones[4]. This suggest that cell geometry is closely tied to the length scale of the lateral transport and the strength of the coupling between attachment/detachment zones[4].

However, to answer the question if higher modes become linearly unstable as particle densities are varied, and the consequent effects on the long-time behavior of the system, geometry does not play a major role. Therefore, this work will focus on a first order approximation via a 2D box geometry. Conveniently this geometry simplifies LSA by making it much easier to find the eigenfunctions of the linearized system.

2.2. Linear Stability Analysis (LSA) and Simulation

2.2.1. Purpose of LSA

Solutions of the reaction-diffusion equations (see Eq.2.1-2.5) are the patterns. However, nonlinear systems are hard to solve analytically. Only numerical solutions are feasible, but due to the large parameter space it is computationally very expensive to randomly simulate the system and look for solutions i.e. the formation of patterns.

The idea behind LSA is to find the stationary homogeneous solutions in the parameter space and study the time evolution of small perturbations with respect to these stationary starting states. Fixed points with growing modes are good candidates to turn into a pattern.

Lets have a look at the procedure for an arbitrary system. The reaction-diffusion equation are complemented by reactive boundary condition on the membrane. In the box geometry the normal vector is in the z-direction:

$$\partial_t u_i = D\nabla_z^2 u_i + f_i(\mathbf{u}) \tag{2.13}$$

$$D\nabla_z u_i\big|_{z=0} = f_i(\mathbf{u}) \tag{2.14}$$

with $i \in [de, d, DD, DT, E]$.

The particle density vector is given by $\mathbf{u} = \begin{bmatrix} u_{de} \\ u_d \\ u_{DD} \\ u_{DT} \\ u_E \end{bmatrix}$.Note that u_{de} and u_d live on the membrane and u_{DD}, u_{DT} and u_E in the cytosol.

Generic non-linear functions are given by $\mathbf{f} = \begin{bmatrix} f_{de} \\ f_d \\ f_{DD} \\ f_{DT} \\ f_E \end{bmatrix}$. These functions take the density vector $\mathbf{u}$ as input.

1. **Homogeneous Solutions**

   These homogeneous steady state solutions are found if the system is uniform ($\nabla_z^2 u_i = 0$) and in equilibrium ($\partial_t u_i = 0$) thus Eq.2.13 reads:

$$f_i(\mathbf{u}^*) = 0 \tag{2.15}$$

The fixed points $\mathbf{u}^* = \begin{bmatrix} u^*_{de} \\ u^*_d \\ u^*_{DD} \\ u^*_{DT} \\ u_{E^*} \end{bmatrix}$ are by definition space and time independent. Homogeneous steady state solutions need to satisfy global mass conservation (see Eq.2.12).

$$\begin{aligned} N_D &= u^*_{DD} + u^*_{DT} + \frac{u^*_d + u^*_{de}}{h} \\ N_E &= \frac{u^*_E + u^*_{de}}{h} \end{aligned} \tag{2.16}$$

As a consequence, the infinite dimensional solution space is reduced to a five dimensional solutions space spanned by $\mathbf{u}^*$.

2. **Linearization of the System**
$f_i(\mathbf{u})$ from Eq.2.13 and Eq.2.14 are both linearized by Taylor expanding around the fixed point $\mathbf{u}^*$ to the first order.

$$\begin{aligned} f_i(\mathbf{u}) &\approx \overbrace{f_i(\mathbf{u})\big|_{\mathbf{u}=\mathbf{u}^*}}^{f_i(\mathbf{u}^*)=0} + \overbrace{\partial_{\mathbf{u}} f_i(\mathbf{u})}^{\underline{\mathbf{J}}}\Big|_{\mathbf{u}=\mathbf{u}^*} \cdot \delta(\mathbf{u}) + h.o. \\ &\approx \underline{\mathbf{J}}\big|_{\mathbf{u}=\mathbf{u}^*} \cdot \delta(\mathbf{u}) \end{aligned} \tag{2.17}$$

With Eq.2.17 in mind, Eq.2.13 and Eq.2.14 can be rewritten as a linear system:

$$\left.\begin{aligned} D_m \nabla_z^2 u_i + \underline{\mathbf{J}}\big|_{\mathbf{u}=\mathbf{u}^*} \cdot \delta\mathbf{u} - \partial_t u_i = 0 \\ D_c \nabla_z u_i\big|_{z=0} - \underline{\mathbf{J}}\big|_{\mathbf{u}=\mathbf{u}^*} \cdot \delta\mathbf{u} = 0 \end{aligned}\right\} \mathcal{L} \cdot \delta\mathbf{u} = 0 \tag{2.18}$$

3. **Perturbing the Fixed Point**
A small perturbation $\delta\mathbf{u}$ is added to the fixed points $\mathbf{u}^*$

$$\mathbf{u} = \underbrace{\mathbf{u}^*(z)}_{\substack{\text{time and space} \\ \textbf{independent} \\ \text{fixed points}}} + \underbrace{\delta\mathbf{u}(x,z,t)}_{\substack{\text{time and space} \\ \textbf{dependent} \\ \text{perturbation}}} \tag{2.19}$$

The dynamics of perturbation $\delta\mathbf{u}$ can be expanded into Fourier modes via separation of variables. In order to use the method of separation of variables we must be working with linear homogeneous partial differential equations with linear homogeneous boundary conditions. The advantage of the solution via a separation ansatz is that it reduces the

partial differential equation down to ordinary differential equations which are usually easier to solve.

$$\delta\mathbf{u}(x,z,t) = \sum_q \delta\widetilde{\mathbf{u}}^q e^{\sigma_q t} cos(qx)\zeta(z,q) \tag{2.20}$$

The bulk functions $\zeta(z,q)$ can be obtained analytically and the Fourier coefficient $\delta\widetilde{\mathbf{u}}^q$ are dependent on the wave number q.

Putting Eq.2.20 into Eq.2.19, the perturbed fixed points are then inserted into the linearized system Eq.2.

Note that the time and space independence of $\mathbf{u}^*$ reduces the linear system to

$$\left.\begin{aligned} D\nabla_z^2\,\delta\widetilde{\mathbf{u}}^q + \underline{\mathbf{J}}\big|_{\mathbf{u}=\mathbf{u}^*}\cdot\delta\widetilde{\mathbf{u}}^q - \partial_t\delta\widetilde{\mathbf{u}}^q = 0 \\ D\nabla_z\delta\widetilde{\mathbf{u}}^q\big|_{z=0} - \underline{\mathbf{J}}\big|_{\mathbf{u}=\mathbf{u}^*}\cdot\delta\widetilde{\mathbf{u}}^q = 0 \end{aligned}\right\} \mathcal{L}_q\cdot\delta\widetilde{\mathbf{u}}^q = 0 \tag{2.21}$$

4. **Solving the Eigenvalue Problem of $\mathcal{L}_q$**
   To solve the eigenvalue problem, the characteristic equation of $det(\mathcal{L}_q - \alpha\mathbb{1}) = 0$ has to be solved. Since this matrix is non algebraic, solutions can only be calculated numerically. Solving the eigenvalue problem of the linear system yields a dependence of $\sigma(q)$ called the Dispersion Relation.

   The dispersion relation is a relation between growth rate σ and wave number q. The maximum of the growth rate $\sigma(q_{max})$ can be extracted from solving the characteristic equation from above. Since the perturbation grows exponentially, the largest eigenvalue dominates over all other modes. The aim of this work is to find a change in the largest integer modes that fit into the box geometry. Only considering integer modes, the dispersion relation $\sigma(q)$ can be rewritten in terms of the mode number n with $n \in \mathbb{N}^*$. The dispersion relation can be rewritten to only take integer modes into considerations such that $\sigma(n)$ with

$$q = \frac{2\pi\cdot n}{L} \rightarrow n = \frac{q\cdot L}{2\pi} \tag{2.22}$$

   a) A *stable* fixed point will relax back to its original state if it is perturbed i.e. $Re[\sigma(n = 0)] = 0$.

   b) A fixed point is said to be *unstable* if at least one eigenvalue $Re[\sigma(n)] > 0$.
   In this case the perturbation will grow in the direction of the eigenvector corresponding to the positive eigenvalue.

2.2.2. Simulation and Parameters

LSA is very useful in finding starting points in this large parameter regime which are likely to turn into patterns. However, LSA only provides candidate parameter configurations but in order to make sure these instabilities lead to a pattern, a numerical simulation has to be performed.

The reaction-diffusion equations for the Min-system are highly nonlinear, therefore the choice of parameters for LSA and the simulation is crucial. The diffusion coefficients D_c and D_m as well as the lower bound of the nucleotide exchange rate λ were experimentally determined[6][12]. The kinetic rate constants were adjusted and modulated to obtain spatial patterns in simulations.

The set of *in vivo* parameters for this work were provided by Laeschkir Würthner[9].

Test-parameters	**Symbol**	**Value**
Cytosolic Diffusion Constant	D_c	60 $\mu m^2 s^{-1}$
Membrane Diffusion Constant	D_m	0.013 $\mu m^2 s^{-1}$
MinD-ATP attachment rate	k_D	0.065 $\mu m s^{-1}$
MinD-ATP recruitment rate	k_{dD}	0.025 $\mu m^3 s^{-1}$
MinE recruitment rate	k_{dE}	0.126 $\mu m^3 s^{-1}$
MinDE-complex detachment rate	k_{de}	0.34 s^{-1}
Nucleotide exchange rate	λ	6 s^{-1}
Length of mayor axis	L	10 μm
Height of cytosol (Box model)	h	5 μm

Table 2.1.: Table of Test-parameters used in LSA and simulation

The LSA for the skeleton model of the Min-system in a 2D Box was implemented in Python using SymPy[13], NumPy[14] and Matplotlib[15] libraries. The corresponding simulations were implemented in Comsol software version 5.4[16].

3. Results

3.1. Phase Space

To investigate how the skeleton model behaves under changes of MinE/MinD denisity ratios, lets look at the 2D phase space spanned by the two conserved global mass densities of $minE$ and $minD$. The essential assumption is that the distribution of proteins is homogeneous. This means that all membrane and bulk species as well as the global mass densities are constant in space and are therefore independent of the geometry. Taking the 2D box geometry of Fig2.2 into account where $\int_\Omega dc = L \cdot h$ and $\int_{\delta\Omega} dm = L$, the global mass densities are related to the total number of MinD and MinE as such:

$$\begin{aligned} N_D &= \int_\Omega dc\, minD = minD \cdot L \cdot h \\ N_E &= \int_\Omega dc\, minE = minE \cdot L \cdot h \end{aligned} \tag{3.1}$$

In the same way Eq.2.12 can be rewritten:

$$\begin{aligned} N_D &= L \cdot h(\widetilde{u}_{DD} + \widetilde{u}_{DT}) + L(\widetilde{u}_d + \widetilde{u}_{de}) \\ N_E &= L \cdot h \cdot \widetilde{u}_E + L \cdot \widetilde{u}_{de} \end{aligned} \tag{3.2}$$

From Eq.3.1 and Eq.3.3 the global mass densities are defined as:

$$\begin{aligned} minD &= \widetilde{u}_{DD} + \widetilde{u}_{DT} + \frac{\widetilde{u}_d + \widetilde{u}_{de}}{h} \\ minE &= \widetilde{u}_E + \frac{\widetilde{u}_{de}}{h} \end{aligned} \tag{3.3}$$

where the membrane species u_{de} and u_d can be re-scaled by the bulk height h. Due to the homogeneous distribution, the global densities and total number of MinD and MinE are directly proportional (see Eq.3.1). Scaling the global densities directly translates to proportional scaling of the total number of particles.

3.2. The Bistable Regime

3.2.1. Control Parameters Σ and Δ

In order to investigate how changes of MinE/MinD denisity ratios influence pattern formation in the mass conserving reaction diffusion system of the skeleton model, two control parameters Σ and Δ are introduced. Control parameters are the local values of globally conserved

quantities (global mass densities from Eq.3.3). The control parameters capture higher order properties of the system.

1. Spatio-temporal dynamics of the Min-oscillations result from lateral instabilities caused by the accumulation/depletion of attachment/detachment zones on the membrane. Accumulation is a result of recruitment due to an abundance of MinD and detachment occurs when there is more MinE than MinD. The denisity ratios of MinE to MinD are therefore chosen as control parameters to describe this dynamic.

$$\Delta = \frac{minE}{minD} \tag{3.4}$$

2. The second control variable is a measure for the relative change of the joint global mass densities of both MinE and MinD.

$$\Sigma = \frac{minE + minD}{2} \tag{3.5}$$

The global mass densities from Eq.3.3 can be expressed in terms of the control parameters (see Fig.3.1):

$$minE = \frac{2\Delta\Sigma}{1+\Delta} \quad \text{and} \quad minD = \frac{2\Sigma}{1+\Delta} \tag{3.6}$$

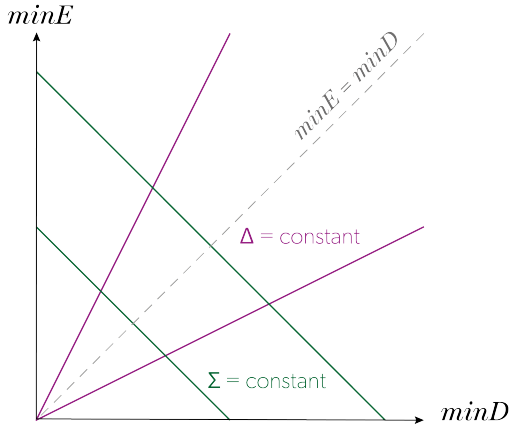

Figure 3.1.: The control space is spanned by conserved mass densities $minD$ and $minE$. The sum of the two global mass densities is kept fixed if Σ is fixed. Varying Δ over constant values between 0 and 1 sweeps the control space for bistable regimes.

3.2.2. Pattern Formation and Bistabiliy

For the theoretical study on pattern-forming systems the geometric analysis of the phase-space structure of mass-conserving reaction–diffusion systems is crucial. The generic bifurcation

scenario underlying any pattern-forming two-component mass conserving reaction diffusion system is a cusp bifurcation[10]. In other words, patterns form at the transition point between one-fixed-point regimes and three-fixed-point regimes for particular values of global densities.

To get an intuition for the connection between pattern formation and a cusp bifurcation, lets look at the membrane bound proteins u_{de} and u_d that make up the spatio-temporal patterns. First, Σ is fixed to be constant. Second, Δ is varied from 0 to 1. Plotting the fixed point for each combination of $u_{de} + u_d$ and Δ results in a typical S-shaped reactive nullcline (line of chemical equilibria) as seen in Fig.3.2. The grey line segments representing stable fixed points and the blue segment represent unstable fixed points. In control space, the bistable regime describes the system exhibiting three fixed points: two stable and one unstable, for each combination of the control parameters.

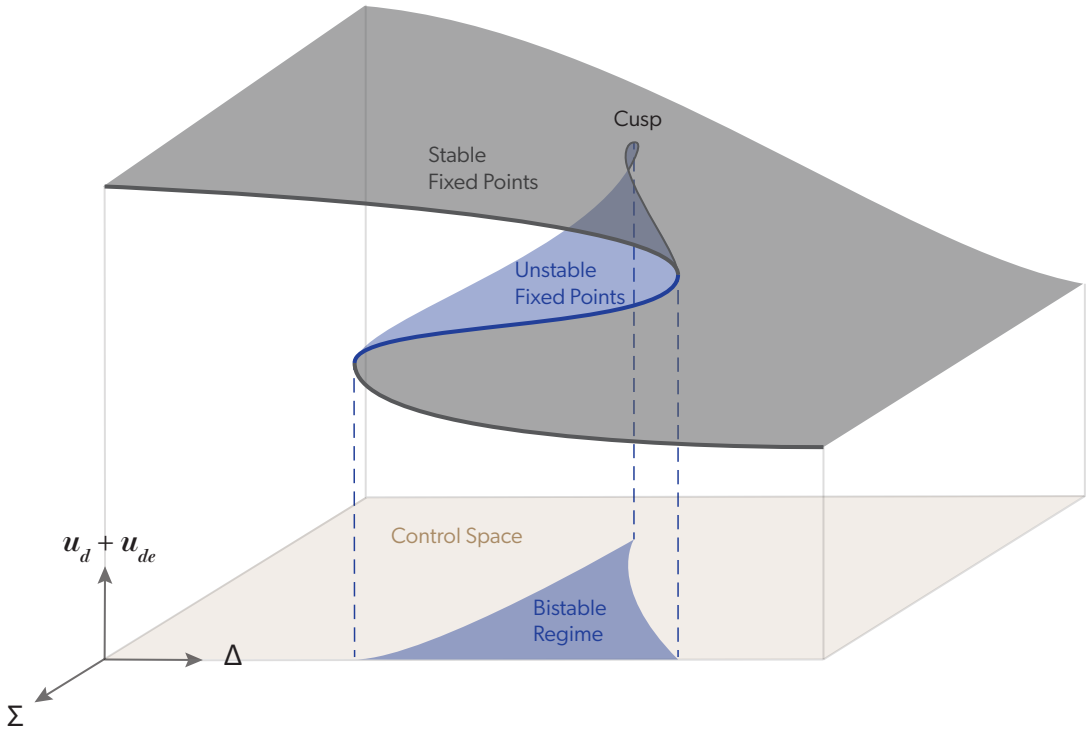

Figure 3.2.: S-shaped reactive nullcline results from plotting the fixed points of the reactive membrane species against different values of Δ . Grey line segment: stable fixed points; Blue line segment: unstable fixed points. In control space (brown), the bistable regime (blue) represents the system exhibiting three fixed points, two stable one unstable.

By changing Σ, one can imagine vertically slicing through the plane of equilibrium fixed points in search for a bistable regime promising parameter sets that turn into patterns. Unstable fixed points in the blue region can turn into patterns if they are homogeneously perturbed. The so called cusp can be seen in control space when the one-fixed-point regime turns into a three-fixed-point regime.

3.2.3. Cone

Switching back to the reduced phase space spanned by the densities $minE$ and $minD$, this very same structure looks like a cone (see Fig.3.4). Its shape is highly dependent on the system parameters. For example, the value of k_{dE} has an influence on the width of the cone. Increasing the MinE detachment rate k_{dE} means the system becomes more stable which is reflected in the number of bistable fixed points that make up the cone. Other system parameters also influence the shape by making the system more or less susceptible to perturbations e.g. global densities and the length of the system.

The skeleton model only allows Turing instabilities when the ratio of $minE/minD < 1$, which means that the cone can only be found in the bottom of the diagonal in the reduced phase space (see Fig.3.1).

For a set of particular parameters (table 2.1) there is a different number of fixed points per combination.

The system has one stable fixed point everywhere, however, the space can be divided into three distinct regions of interest:

1. **Blue points**
   For specific denisity ratios of $minE/minD$ there is a region where the system has 3 stationary homogeneous solutions. In the three-fixed-point regime there are two fixed points which are stable against homogeneous perturbations, whereas the third fixed point is unstable, analogously to the two grey line segments and the one blue line segment that make up the bistable regime in Fig.3.2. One of the stable fixed points is Turing unstable. Turing unstable fixed points are spatially homogeneous stationary solutions. They are asymptotically stable to spatially homogeneous perturbations but unstable to spatially heterogeneous perturbations. This means that heterogeneous perturbations lead to growing spatial instabilities which are likely to turn into patterns.

2. **Orange points**
   Below the bistable regime (blue cone) there is an adjacent smaller orange cone. This area represents a collection of stable fixed which are Turing unstable.

3. **White area**
   All fixed points outside the cone are stable fixed points.

Of interest are Turing unstable fixed points that are defined by lateral instabilities with locally stable steady states. In the dispersion relation, n_c indicates the fastest growing integer mode and n_{max} the largest integer mode with the shortest wavelength that can fit into the geometry (see Fig.3.4). To check how the change in $minE/minD$ ratio affect patterns, lets look at the maximum modes arising from varying $minE/minD$ rations while maintaining conserved global mass densities. The goal is to find a set of parameter where the fasted growing integer mode denoted by n_c increases solely by changing the $minE/minD$ rations i.e. keeping Σ constant and varying Δ.

One candidate parameter set for such a increase of n_c is found at:

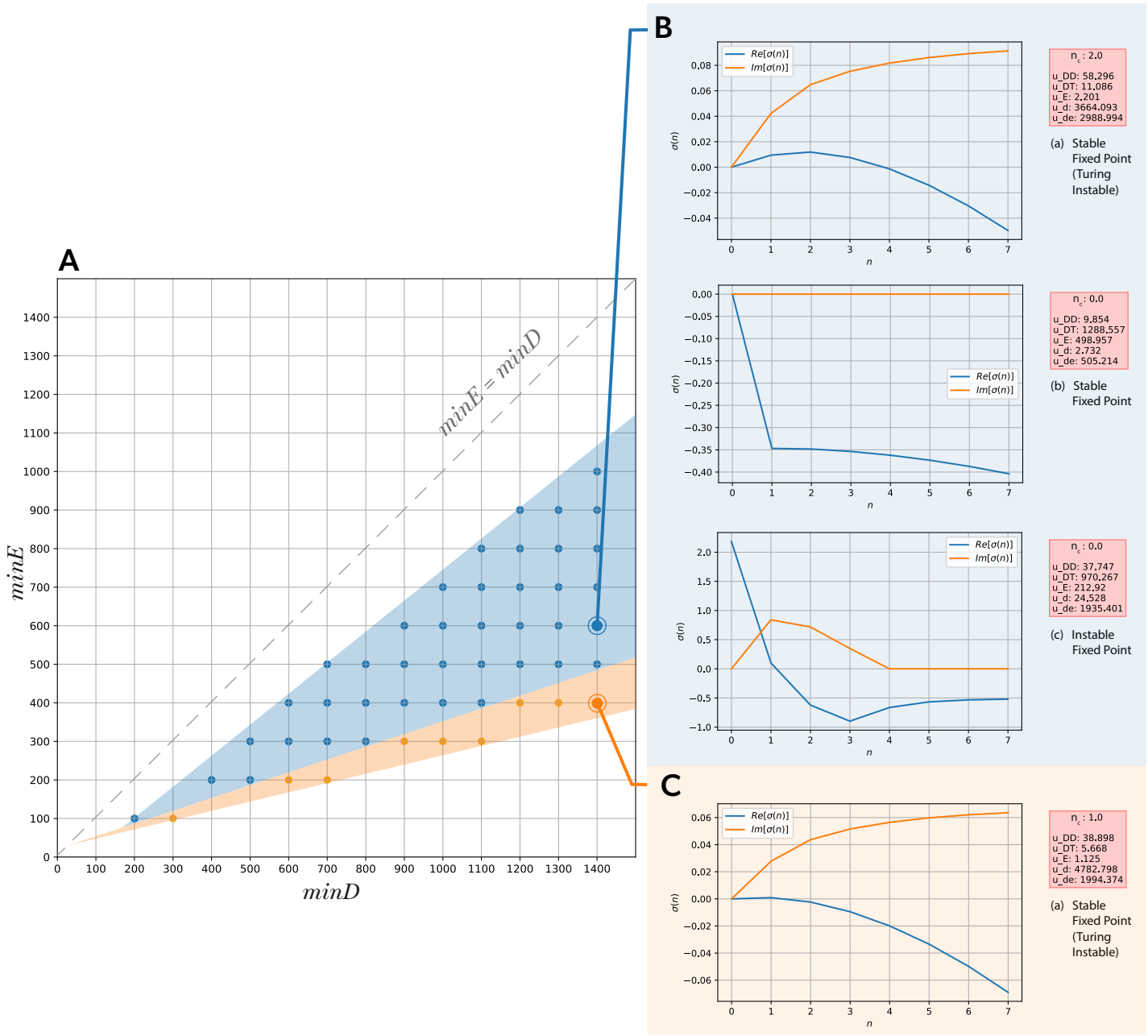

Figure 3.3.: **A** The bistable regime in control space has a cone-like structure. Each point in the blue region represents three fixed points; an unstable fixed point and two stable fixed points where one of them in Turing unstable. The orange area represents a region of Turing unstable fixed points. **B** Sample dispersion relation for the regime of $minE/minD = 600/1400$. This regime has three fixed points. **(a)** Turing unstable fixed points with $n_c = 2$, presumably leading to striped patterns in a simulation. **(b)** Stable fixed point; eigenvalues $Re[\sigma(n = 0)] = 0$ imply that any perturbation just relaxes bacn to the the stable fixed point. **(c)** Unstable fixed point; high $Re[\sigma(n)]$ mean a small perturbation is likely to push this fixed point into the stable or Turing unstable regime. **C** Sample dispersion relation for the regime of $minE/minD = 400/1400$. This regime has one Turing unstable fixed point with a relatively small eigenvalue $Re[\sigma(n)] > 0$. A pattern takes longer to form compared to larger eigenvalues.

$$\Sigma = 1900$$
$$\Delta = \frac{500}{1400} \rightarrow \frac{700}{1200} \tag{3.7}$$

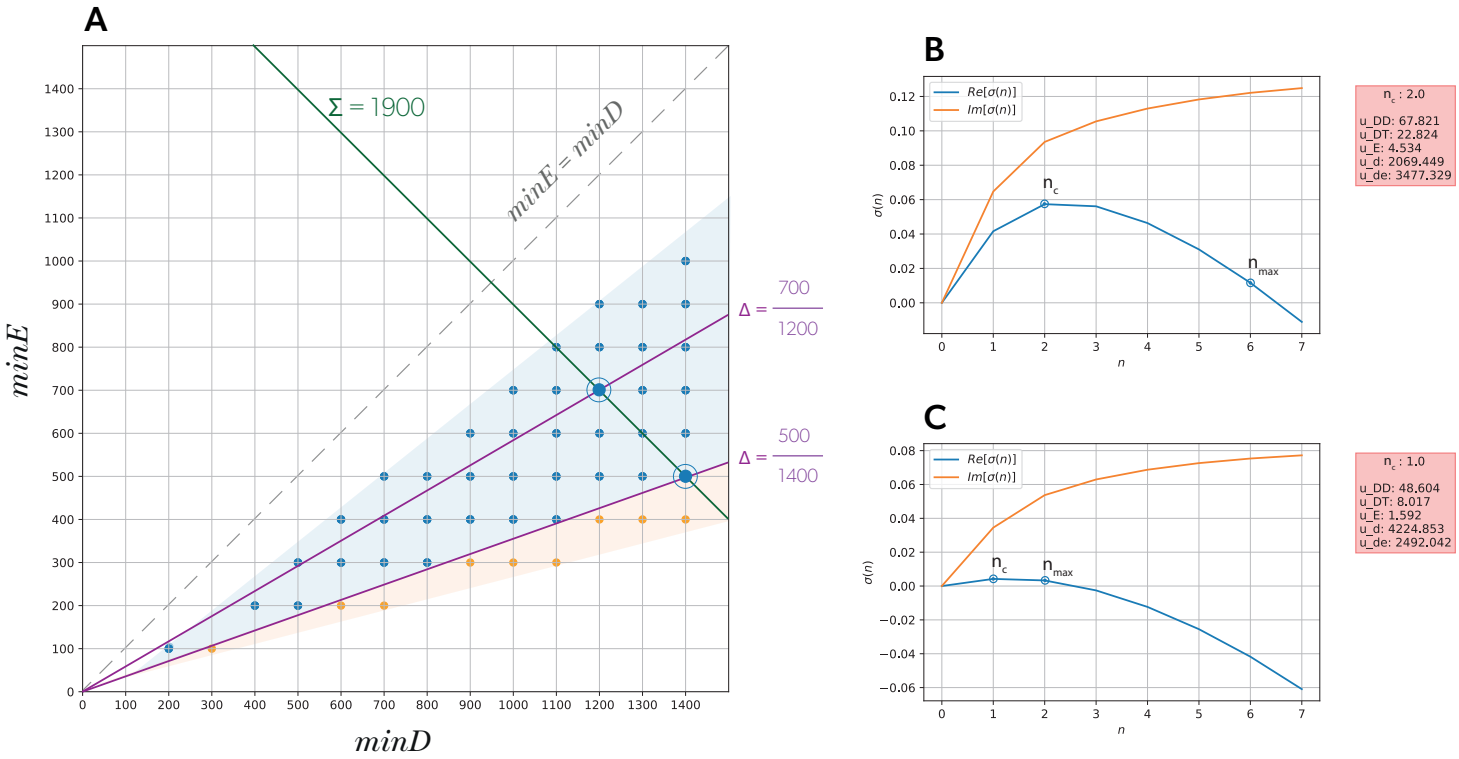

Figure 3.4.: **A** Control space for the special case where the maximum integer mode in the dispersion relation defined by $n_c = 2 \rightarrow n_c = 1$ by solely by changing $minE/minD$ denisity ratios. $\Sigma = 1900$ and $\Delta = 700/1200 \rightarrow \Delta = 500/1400$ **B** Dispersion relation where the larges eigenvalue $Re[\sigma(n)]$ is at $k_c = 2$ **C** Dispersion relation where the larges eigenvalue $Re[\sigma(n)]$ is at $k_c = 1$

Since the dispersion relation obtained by LSA makes no assertions about the pattern formation, these parameter sets are simulated in Comsol software version 5.4.

3.3. Simulation

3.3.1. No-flux Boundary Conditions at $L = 10$

Simulating the parameters from table2.1 the total density of reactive membrane species $u_d + u_{de}$ is plotted against the system length L over a time interval t with no-flux boundary conditions on top and on the sides of the box (see. Fig.3.5).

Note that the time for patterns to form is related to the eigenvalues $\sigma(n)$ such that it takes longer for small eigenvalues to develop into patterns compared to larger values of $\sigma(n)$.

For $n_c = 1$ the pattern exhibits the classic pole-to-pole oscillations that occur if the length of the geometry is equal to wavelength of the mode.

For $n_c = 2$ the system briefly exhibits striped patterns, however they look very asymmetrical. Striped patterns occur when the length of the geometry is equal to twice the wavelength of the dominating mode. This results in higher modes becoming linearly unstable due to changes in particle density ratios. Interestingly, for longer times, there appears to be a transition from the asymmetric oscillations at onset to stable mode-1 oscillations. The origin of this observations are not clear.

3.3.2. No-flux Boundary conditions for $L > 10$

By slightly increasing the system length from $L = 10 \rightarrow L = 10.1$ the mode-2 oscillations predicted by LSA are visible more clearly in the simulation of the membrane species along the major axis (see Fig.3.6 A). However, the striped pattern also looks asymmetrical and indeed cannot sustain itself. The asymmetry in the patter oscillation evolves over time and turns into what could be describes as turbulence before transitioning into pole-to-pole oscillations. The origin of the turbulence, for example by distinguishing between mode coupling or random chaos, could not be determined in work.

To check how robust the system is to changes in length, the major axis was further increased to $L = 15$ (see Fig.3.6 B). At the onset the system exhibits relativity stable striped patterns. The higher modes become linearly unstable due to changes in particle density ratios at onset but no not dominate the long time behaviour. Astonishingly, the skeleton model adapts well to the change and once more transitions from striped patterns into stable pole-to-pole oscillations.

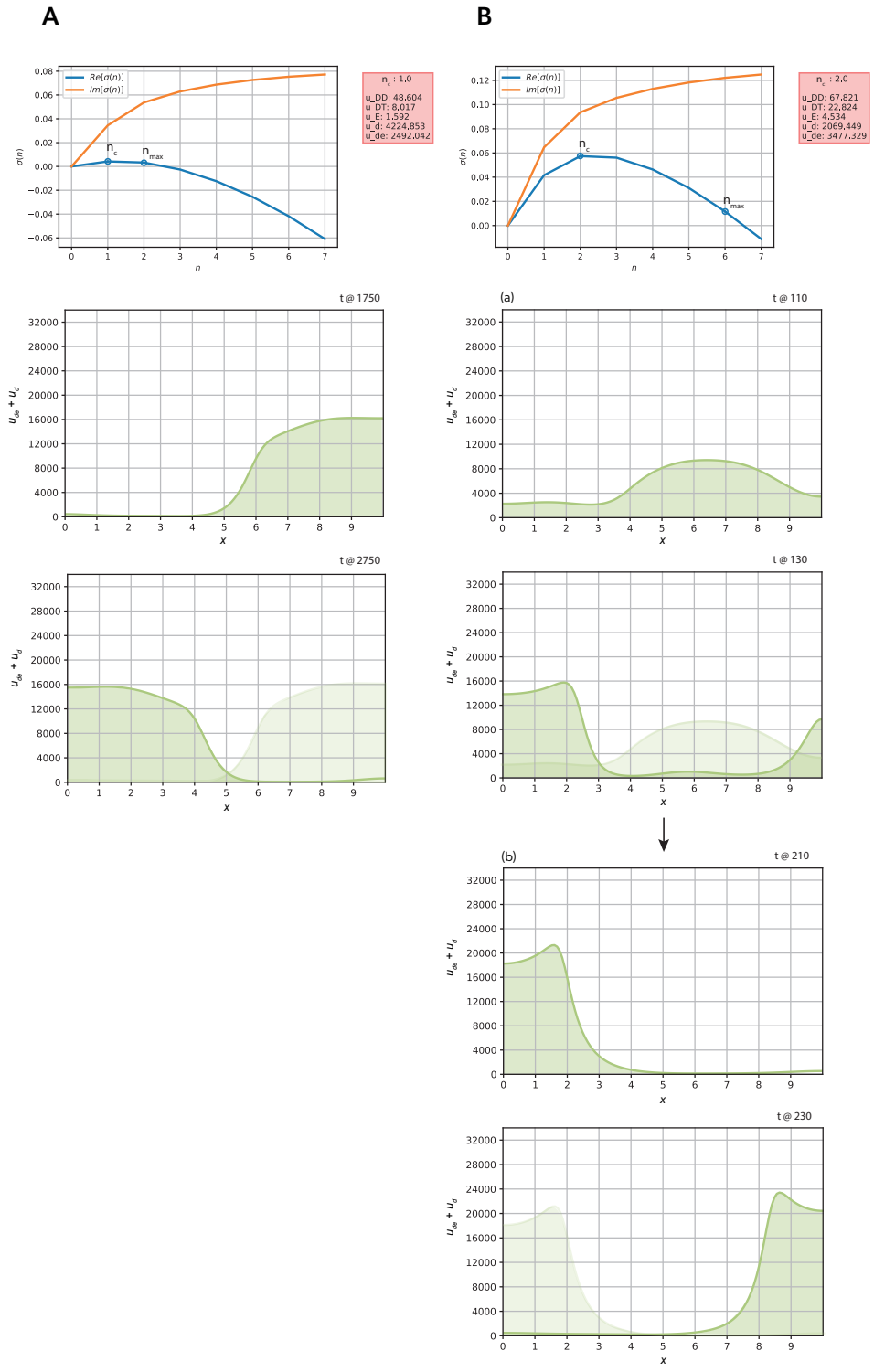

Figure 3.5.: Simulation of the membrane species $u_{de} + u_d$ (green) along major axis over time for $n_c = 1$ and $n_c = 2$ **A** Simulating the fixed point with the largest eigenvalue at $n_c = 1$, the system exhibits pole-to-pole oscillations **B** Simulating the fixed point with the largest eigenvalue at $n_c = 2$, the system exhibits very asymmetrical striped patterns before stabilizing into pole-to-pole oscillations over longer times.

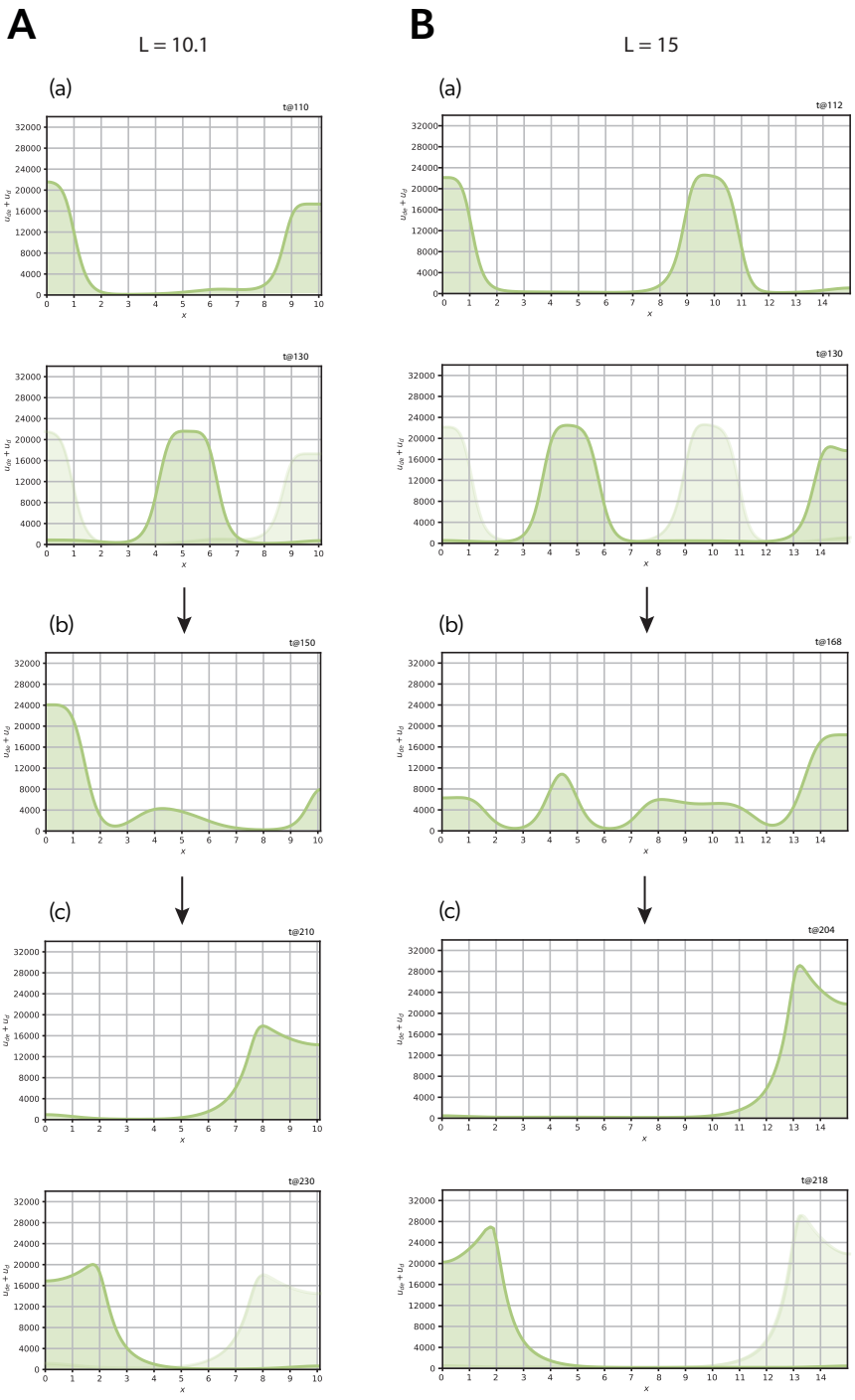

Figure 3.6.: Simulation of the membrane species $u_{de} + u_d$ (green) along major axis over time for $n_c = 2$ at $L = 10.1$ and $L = 15$ **A** Simulating the fixed point with the largest eigenvalue at $n_c = 2$ at a slightly longer system length. **(a)** the system exhibits slightly asymmetrical striped pattern at the onset **(b)** the system becomes turbulent for longer times **(a)** for even longer times the system re-establishes pole-to-pole oscillations **B** Simulating the system at $L = 15$ **(a)** at onset striped patterns form **(b)** for longer times the system becomes unstable and turbulent **(c)** for even longer times the system re-establishes pole-to-pole oscillations

4. Discussion and Outlook

4.1. Discussion

The central finding of this work is that the skeleton model robustly produces pole-to-pole oscillation in the *in vivo* parameter regime under changes in particle denisity ratios. Higher modes become linearly unstable as particle densities are varied, but they do not dominate the long-time behavior of the system.

The membrane species along the major axis were simulated with a particular ratio of particle densities that allow higher modes in the system to become linearly unstable. LSA correctly predicts higher mode patterns at the onset, but it is not suitable to make assertions about the long term behaviour of Min-oscillations as illustrated by Fig.3.5 and Fig.3.6.

The simulation revealed that the system exhibits turbulent behaviour at some point, but over time transitions into pole-to-pole oscillations. Whether the turbulence are an overlay of several modes or random chaos could not be determined as origin of this observations are not clear. The finding that the system transitions from turbulence to stable pole-to-pole oscillations speaks for the robustness of the skeleton model. The purpose of locating the middle of the system is sustained through changes in system length and changes to particle denisity ratios.

The observation that spatially coherent pole-to-pole oscillations are re-established far from the onset might be explained through combined interplay between mutually commensurable, unstable modes in control space[3]. According to the theoretical approach by Halatek at al. to characterize dynamical states arbitrarily far from (global) equilibrium, the transition from turbulence to spatially coherent patterns occurs when the fastest growing mode q_c becomes commensurable with the last unstable mode q_{max}. His numerical approach showed that when $q_{max} \geq 2 \cdot q_c$ chemical turbulence turn into spatially coherent standing wave patterns. In this work, the largest unstable mode and the fastest growing mode defined by their integer mode number and are related as $n_{max} = 3 \cdot n_c$ (see Fig.3.4 B where $n_c = 2$; $n_{max} = 6$) which falls in line with their work. However, the foundations of these observations are only being hypothesized about but not fully understood.

The system length was increased and the simulation showed that the higher modes predicted by LSA become more favorable at onset. However, their asymmetry also results in turbulence which, after some time, re-organizes into stable pole-to-pole oscillations.

An explanation for this observation might be that due to a longer system length, it takes longer for the mass redistribution to hit some critical point that no longer supports higher mode oscillations. Since the sides of the box are no-flux boundaries, the proteins pushed to either side might be stuck and cannot redistribute in time to form a stable pattern.

Changing the boundaries of the sides of the box to be periodic might give some insight into

whether this explanation holds. However it would be important to investigate whether the behaviour is simply an artifact due to the boundary conditions or involves real physics. In case periodic boundaries lead to stable patterns, mass redistribution seems to be a heuristic explanation for why patterns become unstable within no-flux boundaries as the mass pushed to the edges of the system re-enters on the opposite side.

4.2. Outlook

4.2.1. Periodic Boundary Conditions

It would be interesting to further investigate the behaviour of the system of the boundary conditions are changed from no-flux $n = qL/2\pi$ to periodic $n = qL/\pi$. Maybe with periodic boundaries, the particles pushed to the edge of the box and appear on the right side, reduce the accumulated mass on one side and stabilizing the pattern by redistributing them to the opposite side.

4.2.2. Commensurability Condition

Thoroughly checking the commensurability for a wider range of modes might also give insight into whether this condition always holds.

4.2.3. Switch Model

The robustness of Min-oscillations to changes in MinE/MinD density ratios observed in *in vitro*[6][7] cannot be reproduced by the skeleton model. It only produces patterns when the ratio of MinE/MinD < 1. Due to experimental findings[8] Denk[2] proposed an amendment to the switch model by introducing a conformational switch in MinE which allows the model to produce patterns for MinE/MinD > 1. In the cytosol, MinE undergoes conformational changes . It can switch between a reactive state and a latent state at a rate of μ. The reactive state can attach to membrane-bound MinD at a rate $k_{dE,r}$ and the latent state with a lower rate of $k_{dE,l}$ (see Fig.4.1).

The conformational switches of MinE and MinD are interlinked (see Fig.4.2).The switch between latent and reactive MinE is influenced by nearby MinD. Active MinD-ATP triggers the switch from latent MinE to reactive MinE. Similarly, inactive MinD-ADP is affected by the presence of reactive MinE. It triggers MinD ATP activity.

The switch model is equivalent to the skeleton model if

- $\mu \to 0$ and $k_{dE,l} \to 0$ or
- $k_{dE,l} = k_{dE,r}$

Investigating if there is a similar bistable regime in the switch model, I would assume this cone is no longer restricted to the bottom half of the diagonal because the switch model also allows for ratio of MinE/MinD > 1.

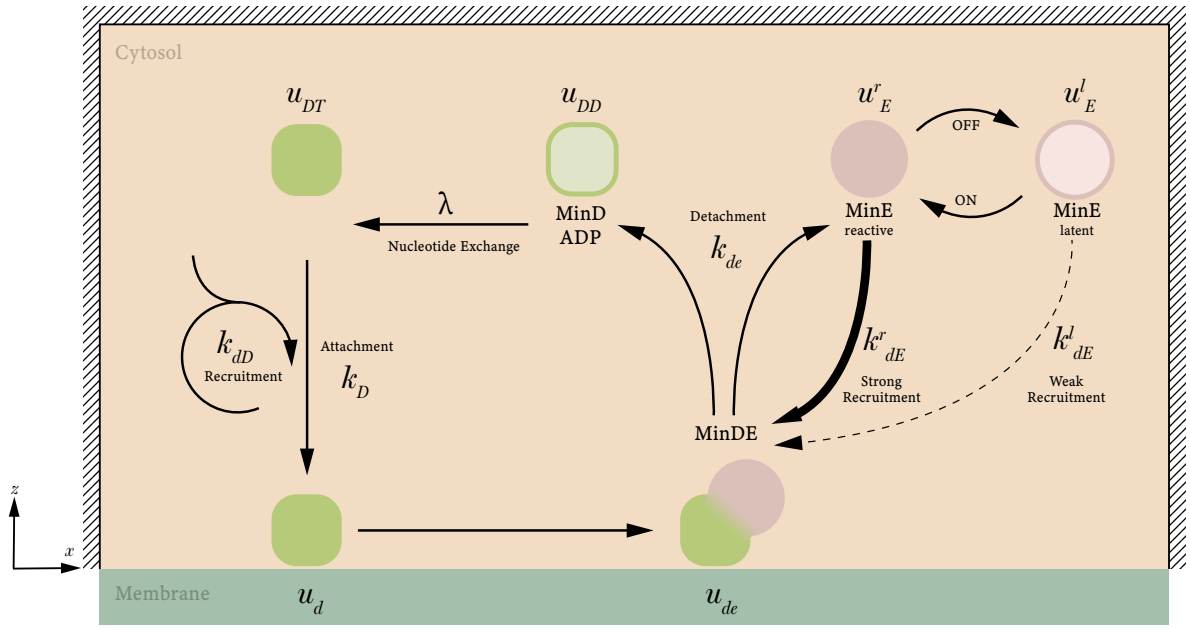

Figure 4.1.: The figure shows a schematic of the switch model for the Min-system in 2D box geometry with no-flux boundary conditions. The accumulation due to attachment and recruitment encounters lateral instabilities as a result of detachment, diffusion and nucleotide exchange and the switch in MinE. This interplay results in spatio-temporal dynamics. All rates and densities are listed in the glossary.

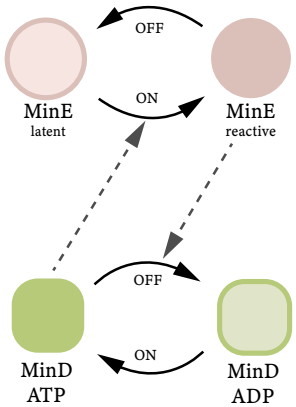

Figure 4.2: Schematic of how conformational switch of MinD and MinE are interlinked. Reactive MinE has an influence on the ATP activity of MinD. At the same time active MinD-ATP triggers more conformational changes from latent MinE to reactive MinE

It would be very interesting to see how the switch model behaves under changes in MinE/MinD density ratios similar to the study of this work.

If the switch model behaves as the skeleton model, this would be evidence that the conformational switch in MinE does not play a mayor role in *in vivo* cells as the reduced skeleton model can sufficiently adapt to changes in particle density ratios.

A. Appendix

A.1. LSA of Skeleton Model in a 2D Box Geometry

The 2D box geometry is used as a simplified approximation. Diffusion and nucleotide exchange can occur everywhere in the 2D cytosol, while all other reactions can only take place at the membrane surface at z=0. The differential equations reads:

For the bulk:

$$\partial_t u_{DD} = D_c \nabla^2 u_{DD} - \lambda u_{DD} \tag{A.1}$$

$$\partial_t u_{DT} = D_c \nabla^2 u_{DT} + \lambda u_{DD} \tag{A.2}$$

$$\partial_t u_E = D_c \nabla^2 u_E \tag{A.3}$$

And for the membrane:

$$\partial_t u_d = D_m \nabla^2 u_d + k_D u_{DT} + k_{dD} u_d u_{DT} - k_{dE} u_E u_d \tag{A.4}$$

$$\partial_t u_{de} = D_m \nabla^2 u_{de} + k_{de} u_E u_d - k_{de} u_{de} \tag{A.5}$$

These equations are complemented by a set of boundary conditions coupling the membrane dynamics to the cytosol.

At the membrane, the requirement is that the flux onto and off the membrane must be equal to the reaction terms that generate that very same flux.

Reactive boundary conditions:

$$D_c \nabla u_{DT} \mid_{z=0} = -u_{DT}(k_D k_{dD} u_d) \tag{A.6}$$

$$D_c \nabla u_{DD} \mid_{z=0} = k_{de} u_{de} \tag{A.7}$$

$$D_c \nabla u_E \mid_{z=0} = k_{de} u_{de} - k_{dE} u_E u_d \tag{A.8}$$

no-flux boundary conditions at top and sides of the box:

$$D_c \nabla u_{DT} \mid_{z=h} = 0 \tag{A.9}$$

$$D_c \nabla u_{DD} \mid_{z=h} = 0 \tag{A.10}$$

$$D_c \nabla u_E \mid_{z=h} = 0 \tag{A.11}$$

A.1.1. Fixed Points

The stationary homogeneous solutions $\widetilde{u}_i$ are found according to the procedure describes in section 2.2.1.

All equation Eq. A.1 are solved in the same manner. Lets look at u_{DD} in detail.

First solve:

$$D_D \nabla^2 \widetilde{u}_{DD} - \lambda \widetilde{u}_{DD} = 0 \tag{A.12}$$

Using the method of separation of variables, for $\widetilde{u}_{DD}$:

$$\widetilde{u}_{DD} = X(x)Z(z)T(t) \tag{A.13}$$

And plugging Eq.A.13 into Eq. A.12 yields:

$$D_D \partial_z^2 [X(x)Z(z)T(t)] = \lambda X(x)Z(z)T(t) \tag{A.14}$$

$$X(x)T(t) \cdot D_D \partial_z^2 Z(z) = X(x)T(t) \cdot \lambda Z(z) \tag{A.15}$$

$$D_D \partial_z^2 Z(z) = \lambda Z(z) \tag{A.16}$$

This is an easily solvable differential equation:

$$Z(z) = Ae^{\sqrt{\lambda/D_D}z} + Be^{-\sqrt{\lambda/D_D}z} \tag{A.17}$$

To determine the constants A and B, lets first exploit the boundary condition at the top, where canonically $z = h$. Employing the substitution $\tilde{z} = h - z$, one is able to apply Eq. A.10 in the following form:

$$[D_D \partial_{\tilde{z}} Ae^{\sqrt{\lambda/D_D}\tilde{z}} + Be^{-\sqrt{\lambda/D_D}\tilde{z}}] \mid_{\tilde{z}=0} = 0 \tag{A.18}$$

Leading to:

$$A = B \Rightarrow \widetilde{u}_{DD}(z) = A\cosh(\sqrt{\lambda/D_D}(h-z)) \tag{A.19}$$

Applying the reactive boundary condition, Eq. A.7:

$$\widetilde{u}_{DD}(0) = A\cosh(h\sqrt{\lambda/D_D}) = \widetilde{u}^*_{DD} \tag{A.20}$$

Eq. A.20 allows to find A and to rewrite $\widetilde{u}_{DD}(z)$ in its final form:

$$\widetilde{u}_{DD}(z) = \widetilde{u}^*_{DD} \frac{\cosh(\sqrt{\lambda/D_D}(h-z))}{\cosh(h\sqrt{\lambda/D_D})} \tag{A.21}$$

With similar arguments and calculus the expressions for the density profiles u_{DT} and u_E is found, namely:

$$\widetilde{u}_{DT}(z) = \widetilde{u}^*_{DT} + \widetilde{u}^*_{DD}(1 - \frac{\cosh(\sqrt{\lambda/D_D}(h-z))}{\cosh(h\sqrt{\lambda/D_D}}) \tag{A.22}$$

$$\widetilde{u}_E(z) = \widetilde{u}^*_E \tag{A.23}$$

A.1.2. LSA

Once again, the system is perturbed around the fixed points. The perturbed variable reads:

$$u_i = u^*_i + \delta u_i \tag{A.24}$$

For the variables $\widetilde{u}_{DD}, \widetilde{u}_{DT}, \widetilde{u}_E$ in the bulk, since the goal is to reproduce those patterns that live in a 2D plane arising by perturbing a z-dependent set of fixed points, the perturbation δu_i needs to be z-dependent too, namely $\delta u_i(x,z,t)$. This can be written in the following form using separation of variables:

$$\delta u_i = T(t)\Phi(x)\zeta(z) \tag{A.25}$$

Again with the use of separation of variables the perturbation can be expanded in terms of Fourier modes. Note that it is just the general form (i.e. time evolution) of the perturbation that has stayed the same; the behavior (eigenvalues) might actually differ.
So the perturbation in now of the form:

$$\delta u_i = \sum_q e^{\sigma t} cos(qx)\zeta(z,q) \tag{A.26}$$

As a relevant example, let's consider once again Eq. A.1. In order to find the function $\zeta(z,q)$, let's plug in the expression for $\widetilde{u}_{DD}$ given by Eq. A.24, resulting in:

$$\partial_t \delta\widetilde{u}_{DD}(x,z,t) = D_D \nabla^2 \delta\widetilde{u}_{DD}(x,z,t) - \lambda\delta\widetilde{u}_{DD}(x,z,t) \tag{A.27}$$

And substituting $\delta\widetilde{u}_{DD}$ with Eq. A.26:

$$\partial_t(e^{\sigma t} cos(qx)\zeta_{DD}(z,q)) = D_D\nabla^2(e^{\sigma t} cos(qx)\widetilde{u}_{DD}(z,q)) - \lambda(e^{\sigma t} cos(qx)\zeta_{DD}(z,q)) \tag{A.28}$$

Where the summation drops because of the orthogonality property of the Fourier modes.

Performing the derivatives the result is:

$$\partial_z^2 \zeta_{DD}(z) = \left(\frac{\sigma}{D_D} + \frac{\lambda}{D_D} + q^2 \right) \zeta_{DD}(z) \tag{A.29}$$

Where:

$$k^2 = \frac{\sigma}{D_D} + \frac{\lambda}{D_D} + q^2 \tag{A.30}$$

Eq A.29 is easily solvable using A.26:

$$\zeta_{DD}(z) = Ae^{kz} + Be^{-kz} \tag{A.31}$$

Let's employ once again the substitution $\tilde{z} = h - z$ and apply the reflective boundary condition to u_{DD} Eq. A.10 at the top of the box, that is now valid for $\tilde{z} = 0$ ($z = h$). Mind that the flux is calculated along the orthogonal direction of the physical boundary of our system, i.e. the $\tilde{z}$-axis.

$$\nabla_{\tilde{z}} (\widetilde{u}_{DD} * (\tilde{z}) + \delta \widetilde{u}_{DD}(x, \tilde{z}, t)) \mid_{\tilde{z}=0} = 0 \tag{A.32}$$

From which it is obtained that:

$$A = B \tag{A.33}$$

Hence it can be written as:

$$\zeta_{DD}(z') = A \cosh(kz') \Rightarrow \zeta_{DD}(z) = A \cosh k(h - z) \tag{A.34}$$

Lets now consider:

$$\zeta_{DD}(0) = A \cosh(kh) := \delta \widetilde{\widetilde{u}}_{DD} \tag{A.35}$$

Hence:

$$A = \frac{\delta \widetilde{\widetilde{u}}_{DD}}{\cosh(kh)} \tag{A.36}$$

So the amplitude $\zeta_{DD}(z)$ reads:

$$\zeta_{DD}(z) = \frac{\delta \widetilde{\widetilde{u}}_{DD} \cosh(k(h - z))}{\cosh(kh)} \tag{A.37}$$

This results in a complete expression for $\delta \widetilde{u}_{DD}$. We proceed the same way with the other two equations and obtain:

$$\zeta_{DT}(z) = (\delta \widetilde{\widetilde{u}}_{DD} + \delta \widetilde{\widetilde{u}}_{DT}) \frac{\cosh(k_1(h - z))}{\cosh(k_1 h)} - \frac{\delta \widetilde{\widetilde{u}}_{DD} \cosh(k(h - z))}{\cosh(kh)} \tag{A.38}$$

$$\zeta_E(z) = \frac{\delta\tilde{\tilde{u}}_E \cosh\left(k_1(h-z)\right)}{\cosh\left(k_1 h\right)} \tag{A.39}$$

With:

$$k_1^2 = \frac{\sigma}{D_D} + q^2 \tag{A.40}$$

The perturber fixed points are inserted into the linearized system Eq.3

Hence the linear system reads $\mathcal{L}_q \cdot \delta\tilde{\mathbf{u}}_q^i = 0$. In the entry $\mathcal{L}_{ij}$ the i-th reactive term f_i is derived with respect to the j-th density function u_j. (With $i, j = DD, DT, E, d, de$)

The eigenvalue problem for this linear system can only be solved numerically.

(A.41)

$$\mathcal{L}_q = \begin{bmatrix} -\frac{D_D}{\sqrt{\frac{D_D}{D_D q^2+\lambda+\sigma}}} \tanh\left(\frac{h}{\sqrt{\frac{D_D}{D_D q^2+\lambda+\sigma}}}\right) & 0 & 0 & 0 & k_{de} \\ -\frac{D_D}{\sqrt{\frac{D_D}{D_D q^2+\sigma}}} \tanh\left(\frac{h}{\sqrt{\frac{D_D}{D_D q^2+\sigma}}}\right) + \frac{D_D}{\sqrt{\frac{D_D}{D_D q^2+\lambda+\sigma}}} \tanh\left(\frac{h}{\sqrt{\frac{D_D}{D_D q^2+\lambda+\sigma}}}\right) & -k_D - k_{dD} u_d - \frac{D_D}{\sqrt{\frac{D_D}{D_D q^2+\sigma}}} \tanh\left(\frac{h}{\sqrt{\frac{D_D}{D_D q^2+\sigma}}}\right) & 0 & -k_{dD} u_{DT} & 0 \\ 0 & 0 & -k_{dE} u_d - \frac{D_E}{\sqrt{\frac{D_E}{D_E q^2+\sigma}}} \tanh\left(\frac{h}{\sqrt{\frac{D_E}{D_E q^2+\sigma}}}\right) & -k_{dE} u_E & k_{de} \\ 0 & k_D + k_{dD} u_d & -k_{dE} u_d & -D_d q^2 + k_{dD} u_{DT} - k_{dE} u_E - \sigma & 0 \\ 0 & 0 & k_{dE} u_d & k_{dE} u_E & -k_{de} - D_{de} q^2 - \sigma \end{bmatrix}$$

A.2. Switch Model

The reaction-diffusion equations for the switch are:

For the bulk:

$$\partial_t u_{DD} = D_c \nabla^2 u_{DD} - \lambda u_{DD} \tag{A.42}$$

$$\partial_t u_{DT} = D_c \nabla^2 u_{DT} + \lambda u_{DD} \tag{A.43}$$

$$\partial_t u_{E,r} = D_c \nabla^2 u_{E,r} - \mu u_{E,r} \tag{A.44}$$

$$\partial_t u_{E,l} = D_c \nabla^2 u_{E,l} + \mu u_{E,l} \tag{A.45}$$

And for the membrane:

$$\partial_t u_d = D_m \nabla^2 u_d + k_D u_{DT} + k_{dD} u_d u_{DT} - (k_{dE,l} u_{E,l} + k_{dE,r} u_{E,r}) u_d \tag{A.46}$$

$$\partial_t u_{de} = D_m \nabla^2 u_{de} + u_d (k_{dE,l} u_{E,l} + k_{dE,r} u_{E,r}) - k_{de} u_{de} \tag{A.47}$$

These equations are complemented by a set of boundary conditions coupling the membrane dynamics to the cytosol.

At the membrane, the requirement is that the flux onto and off the membrane must be equal to the reaction terms that generate that very same flux.

Reactive boundary conditions:

$$D_c \nabla u_{DT} \mid_{z=0} = -u_{DT} (k_D k_{dD} u_d) \tag{A.48}$$

$$D_c \nabla u_{DD} \mid_{z=0} = k_{de} u_{de} \tag{A.49}$$

$$D_c \nabla u_{E,r} \mid_{z=0} = k_{de} u_{de} - k_{dE,r} u_{E,r} u_d \tag{A.50}$$

$$D_c \nabla u_{E,l} \mid_{z=0} = -k_{dE,l} u_{E,l} u_d \tag{A.51}$$

no-flux boundary conditions at top and sides of the box:

$$D_c \nabla u_{DT} \mid_{z=h} = 0 \tag{A.52}$$

$$D_c \nabla u_{DD} \mid_{z=h} = 0 \tag{A.53}$$

$$D_c \nabla u_{E,r} \mid_{z=h} = 0 \tag{A.54}$$

$$D_c \nabla u_{E,l} \mid_{z=h} = 0 \tag{A.55}$$

Same as in the skeleton model mass conservation applies so

$$\begin{aligned} N_D &= \int_\Omega dc(\widetilde{u}_{DD} + \widetilde{u}_{DT}) + \int_{\delta\Omega} dm(\widetilde{u}_d + \widetilde{u}_{de}) \\ N_E &= \int_\Omega dc(\widetilde{u}_{E,r} + \widetilde{u}_{E,l}) + \int_{\delta\Omega} dm\widetilde{u}_{de} \end{aligned} \tag{A.56}$$

The procedure for LSA is exactly the same for the switch model as for the skeleton model. The linear system reads:

(A.57)

$$\mathcal{L}_q = \begin{bmatrix} -\frac{D_{,D}\tanh\left(\frac{h}{\sqrt{\frac{D_Q}{D_{QP}^{++}}}\sqrt{D_{QP}^{++}}}\right)}{\sqrt{\frac{D_Q}{D_{QP}^{++}}}} & 0 & 0 & 0 & k_{de} \\ 0 & -\frac{D_{,D}\tanh\left(\frac{h}{\sqrt{\frac{D_Q}{D_{QP}^{++}}}\sqrt{D_{QP}^{++}}}\right)}{\sqrt{\frac{D_Q}{D_{QP}^{++}}}} & 0 & 0 & -k_{dD}u_{DT} \\ 0 & 0 & -\frac{D_{,D}\tanh\left(\frac{h}{\sqrt{\frac{D_Q}{D_{QP}^{++}}}\sqrt{D_{QP}^{++}}}\right)}{\sqrt{\frac{D_Q}{D_{QP}^{++}}}} - k_D - k_{dD}u_d & 0 & 0 \\ 0 & 0 & 0 & -\frac{D_{,E}\tanh\left(\frac{h}{\sqrt{\frac{D_E}{D_{EP}^{++}}}\sqrt{D_{EP}^{++}}}\right)}{\sqrt{\frac{D_E}{D_{EP}^{++}}}} - k_{dE}u_d & -k_{dE}u_{Er} \\ 0 & 0 & 0 & -k_{dE}u_d & -\frac{D_{,E}\tanh\left(\frac{h}{\sqrt{\frac{D_E}{D_{EP}^{++}}}\sqrt{D_{EP}^{++}}}\right)}{\sqrt{\frac{D_E}{D_{EP}^{++}}}} - k_{dE}u_d \\ 0 & 0 & k_D + k_{dD}u_d & k_{dE}u_d & k_{dE}u_d \\ 0 & 0 & 0 & 0 & 0 \end{bmatrix}$$

$$\begin{bmatrix} 0 & 0 \\ -k_{dE}u_{EI} & 0 \\ -D_m q^2 + k_{dD}u_{DT} - k_{dE}u_{EI} - k_{dE}u_{Er} - & -D_m q^2 - k_{de} - \\ k_{dE}u_{EI} + k_{dE}u_{Er} & \end{bmatrix}$$

List of Figures

Glossary

D_c : Diffusion coefficient of MinE and MinD in the cytosol (experimentally determined).. 12

D_m : Diffusion coefficient of MinE and MinD on membrane (experimentally determined).. 12

k_D : Attachment rate with which cytosolic MinD-ATP bind to the membrane (not experimentally determined).. 12

k_{dD} : Recruitment rate with which membrane bound MinD-ATP recruits more MinD-ATP from the cytosol to bind to the membrane and form a polar zone (not experimentally determined).. 12

k_{dE} : Rate with which cytosolic MinE binds to membrane bound MinD-ATP to form a MinDE-complex (not experimentally determined).. 12

k_{de} : Detachment rate with which MinD-ADP and MinE cycle back into the cytosol (not experimentally determined).. 12

$k_{dE,l}$: Rate with which cytosolic latent MinE binds to membrane bound MinD-ATP to form a MinDE-complex (not experimentally determined).. 23

$k_{dE,r}$: Rate with which cytosolic reactive MinE binds to membrane bound MinD-ATP to form a MinDE-complex (not experimentally determined).. 23

λ : Nucleotide exchange rate with which MinD-ADP turn into MinD-ATP (lower bound experimentally determined).. 12

μ : rate with which latent and reactive MinE switch conformational states. 23

u_d : Concentration of membrane bound MinD-ATP. 7

u_{DD} : Concentration of MinD-ADP in the cytosol.. 7

u_{de} : Concentration of membrane bound MinDE-complex.. 7

u_{DT} : Concentration of MinD-ATP in the cytosol.. 7

u_E : Concentration of MinE in the cytosol.. 7

$u_{E,l}$: Concentration of latent MinE in the cytosol.. 32

$u_{E,r}$: Concentration of reactive MinE in the cytosol.. 32

Bibliography

[1] J. Halatek and E. Frey. "Highly Canalized MinD Transfer and MinE Sequestration Explain the Origin of Robust MinCDE-Protein Dynamics". In: *Cell Reports* 1.6 (2012), pp. 741–752. ISSN: 2211-1247. DOI: https://doi.org/10.1016/j.celrep.2012.04.005. URL: http://www.sciencedirect.com/science/article/pii/S2211124712001180.

[2] J. Denk, S. Kretschmer, J. Halatek, C. Hartl, P. Schwille, and E. Frey. "MinE conformational switching confers robustness on self-organized Min protein patterns". In: *Proceedings of the National Academy of Sciences* 115.18 (2018), pp. 4553–4558. ISSN: 0027-8424. DOI: 10.1073/pnas.1719801115. eprint: https://www.pnas.org/content/115/18/4553.full.pdf. URL: https://www.pnas.org/content/115/18/4553.

[3] J. Halatek and E. Frey. "Rethinking pattern formation in reaction–diffusion systems". In: *Nature Physics* 14 (May 2018). DOI: 10.1038/s41567-017-0040-5.

[4] J. Halatek, F. Brauns, and E. Frey. "Self-organization principles of intracellular pattern formation". In: *Philosophical Transactions of the Royal Society B: Biological Sciences* 373.1747 (Apr. 2018), p. 20170107. ISSN: 1471-2970. DOI: 10.1098/rstb.2017.0107. URL: http://dx.doi.org/10.1098/rstb.2017.0107.

[5] B. Di Ventura and V. Sourjik. "Self-organized partitioning of dynamically localized proteins in bacterial cell division". In: *Molecular Systems Biology* 7.1 (2011), p. 457. DOI: 10.1038/msb.2010.111. eprint: https://www.embopress.org/doi/pdf/10.1038/msb.2010.111. URL: https://www.embopress.org/doi/abs/10.1038/msb.2010.111.

[6] M. Loose, E. Fischer-Friedrich, J. Ries, K. Kruse, and P. Schwille. "Spatial Regulators for Bacterial Cell Division Self-Organize into Surface Waves in Vitro". In: *Science* 320.5877 (2008), pp. 789–792. ISSN: 0036-8075. DOI: 10.1126/science.1154413. eprint: https://science.sciencemag.org/content/320/5877/789.full.pdf. URL: https://science.sciencemag.org/content/320/5877/789.

[7] S. Kretschmer and P. Schwille. "Pattern formation on membranes and its role in bacterial cell division". In: *Current Opinion in Cell Biology* 38 (2016). Cell architecture, pp. 52–59. ISSN: 0955-0674. DOI: https://doi.org/10.1016/j.ceb.2016.02.005. URL: http://www.sciencedirect.com/science/article/pii/S0955067416300126.

[8] K.-T. Park, W. Wu, K. Battaile, S. Lovell, T. Holyoak, and J. Lutkenhaus. "The Min Oscillator Uses MinD-Dependent Conformational Changes in MinE to Spatially Regulate Cytokinesis". In: *Cell* 146 (Aug. 2011), pp. 396–407. DOI: 10.1016/j.cell.2011.06.042.

[9] L. Würthner. L.Wuerthner@physik.uni-muenchen.de.

[10] F. Brauns, J. Halatek, and E. Frey. *Phase-space geometry of reaction–diffusion dynamics*. 2018. arXiv: 1812.08684 [nlin.PS].

[11] F. Wu, J. Halatek, M. Reiter, E. Kingma, E. Frey, and C. Dekker. "Multistability and dynamic transitions of intracellular Min protein patterns". In: *Molecular Systems Biology* 12 (June 2016), pp. 873–873. DOI: 10.15252/msb.20156724.

[12] G. Meacci, J. Ries, E. Fischer-Friedrich, N. Kahya, P. Schwille, and K. Kruse. "Mobility of Min-proteins in Escherichia coli measured by fluorescence correlation spectroscopy". In: *Physical biology* 3 (Dec. 2006), pp. 255–63. DOI: 10.1088/1478-3975/3/4/003.

[13] A. Meurer, C. P. Smith, M. Paprocki, O. Čertík, S. B. Kirpichev, M. Rocklin, A. Kumar, S. Ivanov, J. K. Moore, S. Singh, T. Rathnayake, S. Vig, B. E. Granger, R. P. Muller, F. Bonazzi, H. Gupta, S. Vats, F. Johansson, F. Pedregosa, M. J. Curry, A. R. Terrel, Š. Roučka, A. Saboo, I. Fernando, S. Kulal, R. Cimrman, and A. Scopatz. "SymPy". In: *PeerJ Computer Science* 3 (Jan. 2017), e103. ISSN: 2376-5992. DOI: 10.7717/peerj-cs.103. URL: https://doi.org/10.7717/peerj-cs.103.

[14] T. E. Oliphant. *A guide to NumPy*. Vol. 1. Trelgol Publishing USA, 2006.

[15] J. D. Hunter. "Matplotlib: A 2D graphics environment". In: *Computing in Science & Engineering* 9.3 (2007), pp. 90–95. DOI: 10.1109/MCSE.2007.55.

[16] S. COMSOL AB Stockholm. In: (2018). URL: www.comsol.com.